Mixing of Azetidinium in Formamidinium Tin Triiodide Perovskite Solar Cells for Enhanced Photovoltaic Performance and High Stability in Air

Efat Jokar,[a, b] Ping-Huan Hou,[a] Sumit S. Bhosale,[a] He-Shiang Chuang,[a] Sudhakar Narra,[a] and Eric Wei-Guang Diau*[a, b]

Overcoming the issue of the stability of tin-based perovskites is a major challenge for the commercial development of lead-free perovskite solar cells. To attack this problem, a new organic cation, azetidinium (AZ), is incorporated into the crystal structure of formamidinium tin triiodide ($FASnI_3$) to form the mixed-cation perovskite $AZ_xFA_{1-x}SnI_3$. As AZ has a similar size to FA but a larger dipole moment, hybrid $AZ_xFA_{1-x}SnI_3$ films exhibit variation in optical and electronic properties on increasing the proportion of AZ. Trifluoromethylbenzene ($CF_3C_6H_5$) serves as antisolvent to fabricate smooth and uniform perovskite films for the devices with an inverted planar heterojunction structure. The device performance is optimized to produce the greatest efficiency at $x = 0.15$ (AZ15), for which a power conversion efficiency of 9.6% is obtained when the unencapsulated AZ15 device is stored in air for 100 h. Moreover, the device retains 90% of its initial efficiency for over 15 days. The significant performance and stability of this device reveal that the concept of mixed cations is a promising approach to stabilize tin-based perovskite solar cells for future commercialization.

Organic-inorganic hybrid halide lead perovskites have taken tremendous strides toward the development of cheap and solution-processable solar cells.[1–3] Despite this progress in perovskite solar cells (PSC), their durability and lead toxicity issues are major obstacles toward their commercialization.[1,4] A simple way to solve the lead toxicity problem is to replace lead with other non-toxic metals, for which the most promising element is tin,[5–8] but tin-based PSC suffer from instability due to oxidation from Sn^{II} to Sn^{IV}.[8–11] Tin oxidation causes tin vacancies in the crystal structure, and results in severe defects in the tin perovskite layer that lead to efficient charge recombination to degrade the device performance.[9–12] Various strategies such as controlling the film morphology,[13,14] using an additive or co-additive[13–19] and varying the perovskite composition[20–26] and crystal structure have been reported.[27–29] Theoretical and experimental results show that the monovalent cation (A^+) in a 3D structure of $ASnI_3$ has a significant effect on the stability of a tin perovskite.[30,31] Although the electronic structure of a tin perovskite is determined with the *s* orbital of tin and the *p* orbital of halides, the size of cation A and the interaction of A inside the inorganic lattice framework can affect the bond angle and bond length, and result in altered electronic and optical properties of the tin perovskite. The size effect of A has been explored: a larger cation A causes a weaker anti-bonding coupling between Sn s orbitals and I p orbitals and a greater energy of formation of Sn vacancies that improve the stability of tin perovskites.[30] Other factors such as dipole moment and hydrogen bonding of cation A with a halide anion in the inorganic lattice should also be considered to affect the electronic structure and the stability of tin-based perovskites. On considering two A cations of similar size and distinct dipole moments, one can study the effect of polarity of the cation. Calculations indicate that the size of azetidinium (AZ; 250 pm) is similar to that of formamidinium (FA; 253 pm); the dipole moments are 2.52 D and 0.60 D for AZ and FA, respectively.[32]

In the present study, we applied a mixed-cation approach to develop highly stable tin perovskites on incorporation of AZ in varied proportions into the $AZ_xFA_{1-x}SnI_3$ structure ($0 \le x \le 0.25$), labeled as AZ0 to AZ25 for $x = 0$–0.25, respectively. The film morphology and the direction of crystal growth were controlled on applying a specific antisolvent (AS), trifluoromethylbenzene ($CF_3C_6H_5$), followed by solvent annealing (SA) at a low pressure. A negligible change of crystal structure but blue-shifted absorption and PL spectra were observed when AZ was incorporated inside the perovskite crystal. A device made of AZ (15% $AZ_{0.15}FA_{0.85}SnI_3$, or AZ15) attained the greatest efficiency, 9.6%, of power conversion (PCE) with the unencapsulated device in air sustaining more than 15 days.

We made several attempts to control the film morphology to obtain an optimal performance for the $AZ_xFA_{1-x}SnI_3$ devices. We first employed ethylenediammonium diiodide ($EDAI_2$ 1%) as a co-additive (10% SnF_2 as additive) to the precursor solution, as reported elsewhere.[14] We then undertook solvent engineering, including both AS and low-pressure SA treatments, to find the best experimental conditions to form the film. On incorporating AZ into the tin perovskite crystal, rapid crystal growth was observed. The antisolvent should hence be injected at an early stage during spin coating, for which the proportion of solvent dimethyl sulfoxide (DMSO) in the precursor solution

[a] Dr. E. Jokar, P.-H. Hou, Dr. S. S. Bhosale, H.-S. Chuang, Dr. S. Narra, Prof. Dr. E. Wei-Guang Diau
Department of Applied Chemistry and Institute of Molecular Science
National Chiao Tung University, 1001 Ta-Hsueh Rd., Hsinchu 30010 (Taiwan)
E-mail: diau@mail.nctu.edu.tw
[b] Dr. E. Jokar, Prof. Dr. E. Wei-Guang Diau
Center for Emergent Functional Matter Science
National Chiao Tung University, 1001 Ta-Hsueh Rd., Hsinchu 30010 (Taiwan)

Supporting information for this article is available on the WWW under https://doi.org/10.1002/cssc.202101475

© 2021 Wiley-VCH GmbH

is large. Traditional antisolvent chlorobenzene (CB) of dipole moment 1.69 D (b.p. 132 °C) was insufficient to carry DMSO from the film while crystal nucleation of the tin perovskite film proceeded. For this reason, we implemented a new antisolvent, trifluoromethylbenzene (or trifluorotoluene, TFT) of dipole moment 2.86 D (b.p. 103 °C), to remove DMSO efficiently, so that uniform nucleation seeds of tin perovskite were produced following a slow crystal growth to form a highly crystalline film (Figure 1a). A more highly uniform and crystalline film was produced with antisolvent TFT than for CB, for which the device performance of the former is expected to be superior to that of the latter. The AZ0 film morphology with TFT as antisolvent was poor with too many pinholes (see the Supporting Information, Figure S1). When the crystal growth became more rapid on introducing the AZ cation, TFT hence helped to wash out the DMSO efficiently to produce sufficient nucleation centers. This rapid growth is related to a strong interaction between highly polar cation AZ and the $[SnI_n]^{2-n}$ framework. The AZ0 film was thus fabricated using CB as antisolvent but TFT as antisolvent for the other AZ samples. The injection of TFT not only altered the film morphology but also affected the film crystallinity. According to the XRD patterns shown in Figure S2, the perovskite film made with TFT has an intensity ratio of (120) over (100) facets greater than that made of CB for the AZ10 sample; this feature becomes more evident for the AZ0 sample, which is not a suitable direction for charge transfer.[33]

As shown in SEM (Figure 1b–g), the grain size decreases with proportion of AZ increasing from $x=0$ to $x=0.25$. The grain size is clearly seen to decrease at larger AZ proportions; a low-pressure SA treatment[34] was hence applied to those films after the AS treatment. The SEM images (Figures 1h–1j) show that the crystal sizes increased significantly for perovskite films with $x=0.15$ to $x=0.25$ (the corresponding size distributions are shown in Figure S3). The treatment combining AS + low-pressure SA caused a preferred orientation of crystal growth more pronounced along plane direction (100) than along (120) (Figure S4). The low-pressure SA approach follows the common solvent annealing method[35,36] but without the additional solvent being placed inside the Petri dish cover so that the small perovskite crystals recrystallized slowly to generate larger crystal grains under the solvent vapor released from the perovskite precursor solution. The preferred orientation along direction [100] facilitates an efficient charge transfer from perovskite to the charge-transport layer. The AZ15 device fabricated with the AS + SA approach has significantly greater J_{sc} than the device made with only the AS approach (Figure S5).

Upon increasing the proportion of AZ in the $AZ_xFA_{1-x}SnI_3$ perovskite structure, the crystal structure was only slightly altered, as shown in Figure 2a for the powder HRXRD patterns

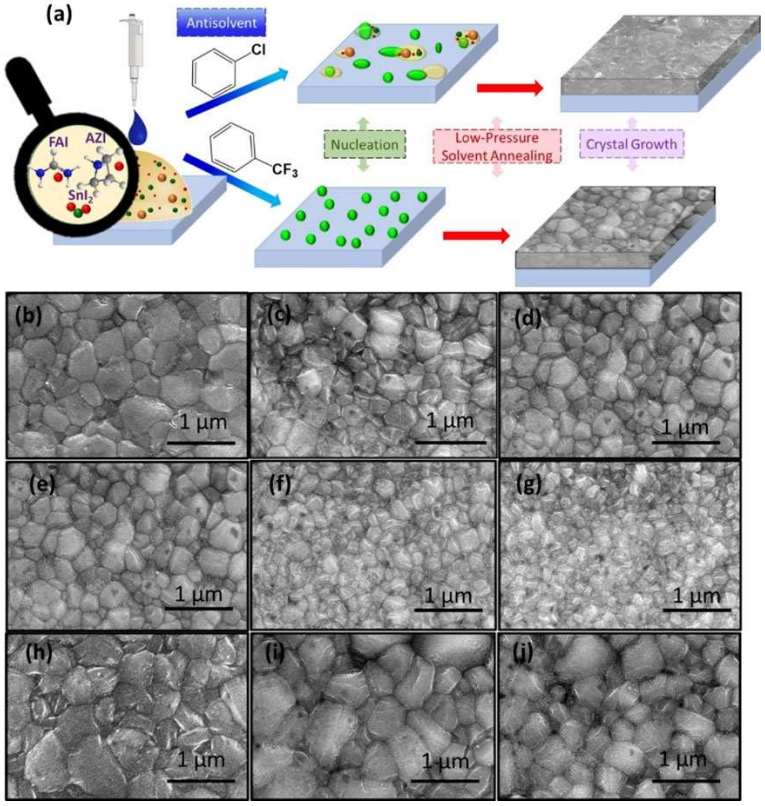

Figure 1. (a) Schematic depiction of the effect of antisolvents chlorobenzene and trifluoromethylbenzene on nucleation followed by solvent annealing at 70 °C and low pressure for the crystal growth of tin perovskite films. (b–g) Top-view SEM images of perovskite films produced after antisolvent treatment for varied ratios of AZ: (b) AZ0; (c) AZ5; (d) AZ10; (e) AZ15M (f) AZ20; (g) AZ25. (h–j) Top-view SEM images showing morphological changes demonstrate the effect of low-pressure solvent annealing: (h) AZ15; (i) AZ20; (j) AZ25.

© 2021 Wiley-VCH GmbH

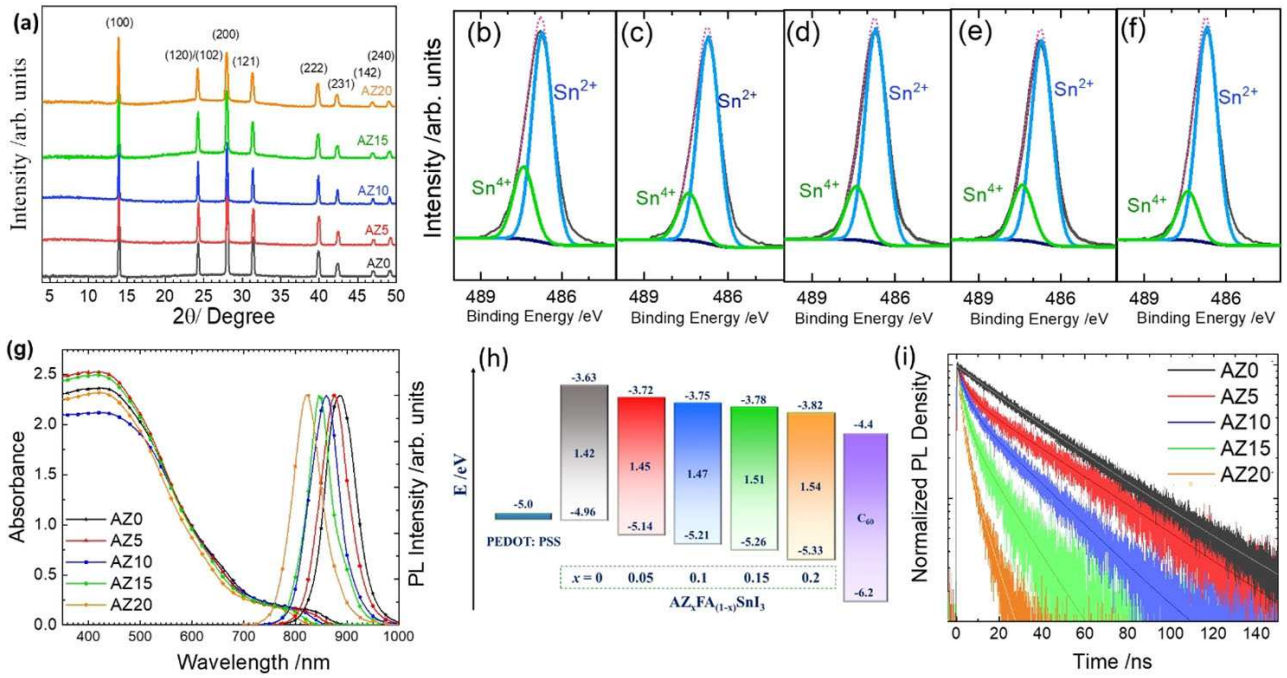

Figure 2. (a) High-resolution X-ray diffraction patterns of AZ films with $x = 0$ (AZ0) to 0.20 (AZ20). (b–f) High-resolution X-ray photoelectron spectra (Sn3d) of the surface of AZ films with $x = 0$ (b), 0.05 (c), 0.10 (d), 0.15 (e), and 0.20 (f). (g) Absorption spectra and steady-state photoluminescence (PL) spectra. (h) Potential-energy diagrams (energies given in eV with respect to vacuum level) obtained from UPS and absorption spectral data. (i) Time-resolved PL profiles obtained from TCSPC measurements of perovskite films on PEDOT:PSS.

of the films, which is consistent with crystallographic data obtained from analysis of a single crystal (Table S1). Diffraction patterns of single crystals of AZ0, AZ10 and AZ15 show that they adopt an orthorhombic unit cell of space group *Amm*2; only slightly increased lattice parameters were observed. The HRXRD patterns of the films with varied AZ proportion ($x = 0$–0.3) were simulated with TOPAS software to calculate the lattice parameters (Figure S6 and Table S2). An additional XRD signal appeared about 10.5° (Figure S6), indicating that a phase separation would occur when the AZ proportion increased above 30%. We found a negligible variation of lattice parameters on introducing AZ into the $FASnI_3$ crystal, which is consistent with the results obtained from single crystals (Table S1). The presence of AZ in AZ15 was confirmed by secondary-ion mass spectrometry (SIMS; Figure S7) and Fourier-transform infrared spectroscopy (FTIR; Figure S8). As the SIMS data show, the AZ and FA cations are distributed uniformly along the AZ15 film. The IR spectrum of AZI salt was compared with those of the AZ perovskite films. The AZI spectrum shows a broad line associated with the N–H stretching vibration at 3150 cm^{-1}; the absorptions of the AZ samples at 1420, 1440, 1280, 1230, and 1160 cm^{-1} are related to N–H deformations and the vibrations of the molecular skeleton, which are strongly coupled with the wagging deformations of the CH_2 groups.[37] The N–H stretching mode of AZ^+ ($x = 0.05$–0.25) about 3150 cm^{-1} showed a significant spectral shift and splitting, which is attributed to the interaction of the azetidinium cation with the anionic sublattice of the perovskite.

To verify the extent of the Sn^{2+}/Sn^{4+} oxidation, we recorded X-ray photoelectron spectra (XPS) for $AZ_xFA_{1-x}SnI_3$ ($x = 0$–0.2) perovskite films (Figure 2b–f). The XPS with introduced AZ became narrowed and shifted to smaller binding energies; the tail in the region of small energy fitted poorly when only Sn^{II} and Sn^{IV} species were considered. The calculated percentages of Sn^{II} and Sn^{IV} species are listed in Table S3. Our XPS results indicate that an incorporation of AZ decreases the proportion of Sn^{IV} even in the case of AZ5, meaning that AZ films have less tendency toward oxidation and fewer surface defects.

UV/Vis absorption and photoluminescence (PL) spectra of $AZ_xFA_{1-x}SnI_3$ films for $x = 0$–0.20 are shown in Figure 2g. The absorption-band edges systematically shifted toward smaller wavelength with increased proportion of AZ; the band-gap energies were determined to be 1.42, 1.45, 1.47, 1.51, and 1.54 eV for $x = 0$, 0.05, 0.10, 0.15 and 0.20, respectively. The corresponding PL spectra follow the absorption spectra in showing a systematic blue-shift feature. Because the size of AZ is similar to that of FA, the crystal structures of the hybrid AZ/FA tin perovskites show only a slightly altered size relative to $FASnI_3$, but the altered optical bandgaps of the mixed cation perovskites are significant; this optical property proves the existence of AZ inside the perovskite crystal structure. AZ is a unique cation with a small size and a large dipole moment that lacks free rotation as has methylammonium (MA) with a small dipole moment. At low temperatures when the rotation of the MA cation was frozen in lead-based perovskite, the dipole alignment of MA cations produces a strong local electric field. This produced internal field eventually increases the bandgap

© 2021 Wiley-VCH GmbH

of MA-ordered orthorhombic domains (Stark-like effect) at low temperatures.[38] In AZ perovskites, the rotation of a highly polar cation is limited even at room temperature. There is thus a local electric field causing the band-gap to become wider in the AZ perovskites.

The electronic structures of perovskites were assessed with ultraviolet photoelectron spectra (UPS). Figure 2h shows the energy levels of the valence-band maxima (VBM) of various samples obtained on analysis of the UPS data (Figure S9); the energy levels of the conduction-band minima (CBM) are derived from scaling the VBM levels with the corresponding band-gap energies. As shown in Figure 2h, the presence of AZ inside the perovskite crystal alters the electronic structure and aligns the energy level of perovskite to an improved match between the HOMO energy level of the hole-transport layer (HTL, PEDOT:PSS) and the LUMO energy level of the electron-transport layer (ETL, C_{60}).

Figure 2i shows transient PL decay profiles of $AZ_xFA_{1-x}SnI_3$/PEDOT:PSS films for $x=0$–0.2. The results indicate that the rate of charge extraction occurring at the perovskite/HTL interface increased with increasing proportion of AZ inside the crystal. Accordingly, the fitted average PL lifetimes (Table S4) decreased from 40.2 to 3.8 ns when the AZ proportion increased from 0 to 0.2. Mixing AZ inside the $FASnI_3$ crystal has hence the effect of accelerating an extraction of charge from perovskite to the HTL layer, which might be rationalized to result from the large dipole moment of AZ generating a localized internal electric field inside the perovskite layer. Although the net field effect of the dipolar AZ cations cancels on a macroscopic scale as they can assume random orientations, microscopically they can still play an important role in charge transport when they are in the proximity of a point defect or at an interface with a hole-transporting layer. It has been shown earlier that alloying an A-site cation with dipolar cations, such as methylammonium, can heal defects and also delocalize the polarons by diminishing their binding energies.[39,40]

The effects of mixing AZ cation on the intrinsic lifetime of the perovskite films studied on glass substrates show that the average PL lifetime of the AZ samples increases with increasing proportion of AZ (Figure S10), attaining a maximum at AZ15, and then decreasing for AZ20. The PL lifetimes of perovskite-only samples were smaller than those of perovskite/PEDOT samples because pinholes existed in the former samples. The increased lifetime of AZ samples with increased AZ content confirms the effects of dipolar cations in healing the defects and delocalizing polarons. The increase of PL lifetime can also be understood in terms of increased polaron size. We also measured the temperature dependence of the PL spectra (Figure S11) to estimate the LO phonon energy. This energy decreased for AZ15 perovskite (44.1 eV) relative to AZ0 (60.1 eV), indicating that the electron-phonon interaction increased in the AZ-based tin perovskite.[40–44]

The $AZ_xFA_{1-x}SnI_3$ films served as light absorbers for photovoltaic applications in an inverted planar heterojunction device configuration ITO/PEDOT:PSS/$AZ_xFA_{1-x}SnI_3$/C_{60}/BCP/Ag. Figures 3a and 3b show the current-voltage curves and the corresponding IPCE spectra for the best cells at AZ proportions $x=0$–0.25, respectively; the corresponding PV parameters of the best cells and their average values are listed in Table S5. The IPCE spectral edge clearly demonstrates a blue shift that is consistent with the absorption spectra shown in Figure 2g. Integration of IPCE over the solar-flux spectrum yielded current densities that agreed well with those obtained from the *J-V* scan curves shown in Figure 3a. Figures 3c–3f show box plots of four PV parameters obtained from 30 identical devices for each AZ cell. Upon increasing the proportion of AZ, a systematically increasing trend of open-circuit voltage (V_{oc}) and fill factor (FF) was observed. In contrast, the short-circuit current density (J_{sc}) maintained similar values at small AZ proportions but decreased at large AZ proportions. The observed variations of J_{sc} and V_{oc} might result from the combined effects of band-gap energies (E_g), band alignment, internal electric field and direction of crystal growth.[44–48] The enhanced V_{oc} is attributed to the band gap that increased with increasing proportion of AZ and based on the electrochemical impedance spectra (EIS) shown in Figure S12. The EIS results confirm that charge recombination was retarded when AZ was involved in the perovskite. As a result, the best performing device appeared at $x=0.15$ (AZ15), for which $J_{sc}=21.7\ mA\,cm^{-2}$, $V_{oc}=0.57$ V, and FF = 0.751, giving PCE = 9.3 %.

The stability of a tin-based PSC is a major challenge to overcome. In the present work, we tested the stability of the best device (AZ15) under severe environmental conditions and compared it with the control device (AZ0). The light-soaking stability of an encapsulated AZ0 and an AZ15 device under one-sun AM1.5G illumination at the point of maximum output in ambient conditions (RH = 50–55 %) was tested. As shown in Figure 3g, both AZ0 and AZ15 devices were stable over 3000 s, but AZ15 was slightly more stable than AZ0 under longer periods of irradiation. The stability of devices stored in darkness was measured under two conditions: with encapsulation stored in a N_2-filled glovebox (Figure 3h) and without encapsulation stored in ambient air with RH = 50–55 % (Figure 3i). Both encapsulated AZ0 and AZ15 devices in a glove box showed great stability over 2000 h with a tendency of slow passivation reported elsewhere.[14,20] In contrast, the unencapsulated AZ15 device showed remarkable stability in ambient air with large relative humidity for over 15 days. The efficiency of AZ15 increased from 8.3 % to a new record, 9.6 %, after storage in air for 100 h (Figure S13), but the AZ0 device showed a rapid decay to zero after 200 h of storage in air. Wang et al.[18] reported using gallic acid and excess $SnCl_2$ to passivate the grain surface of $FASnI_3$ to attain optimal PCE 9.03 %; the unencapsulated device exhibited 80 % of its initial efficiency when exposed to air with RH = 20 % for 1000 h, but the enduring stability of the unencapsulated device stored in air with relative humidity RH > 50 % was still challenging. According to our best knowledge, the stability of unencapsulated AZ15 in air with RH ~ 55 % retaining 90 % of its initial performance for over 15 days (360 h) is the best ever reported. This great stability of AZ15 might be attributed to a strong interaction between highly polar cation AZ and the $[SnI_n]^{2-n}$ framework, which pins them together to avoid a penetration of water and oxygen so as to avoid deterioration of the crystal structure.[49]

© 2021 Wiley-VCH GmbH

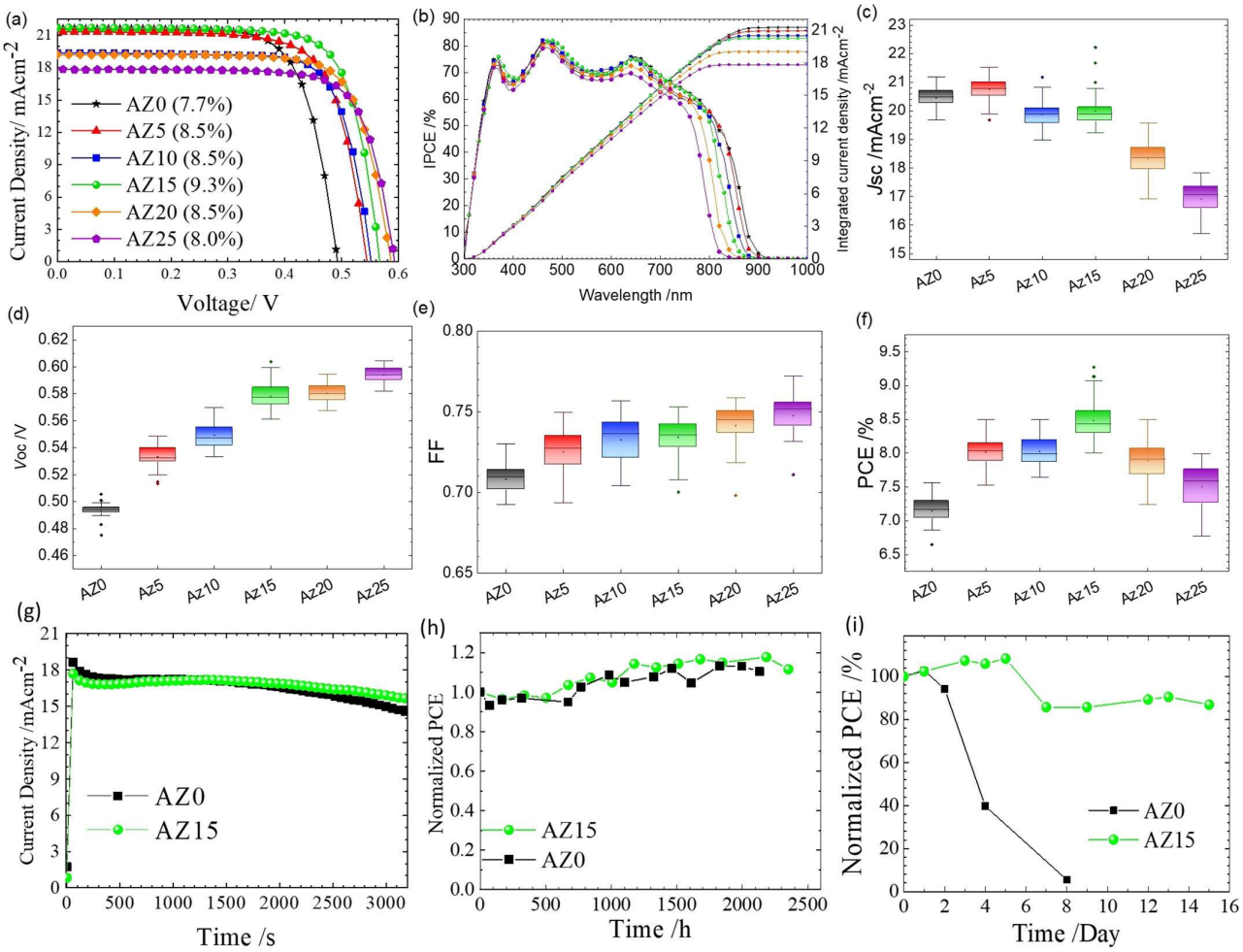

Figure 3. (a) Current–voltage curves and (b) corresponding IPCE spectra with integrated current densities. (c–f) Box plots of photovoltaic parameters of 30 cells fabricated under the same experimental conditions for AZ*x* (*x* = 0–25). (g) Stabilized photocurrent density of AZ0 and AZ15 devices taken at the position of maximum power for one-sun irradiation with an AM 1.5G solar simulator. (h,i) Tests of stability of AZ0 and AZ15 devices as a function of storage period in two environments: (h) encapsulated devices in a N_2-filled glove box; (i) unencapsulated devices in ambient air condition with RH = 50–55 %.

In conclusion, we introduced the organic cation, azetidinium (AZ), cocrystallized in the formamidinium (FA) tin triiodide crystal in various proportions, to form the perovskite $AZ_xFA_{1-x}SnI_3$ (x = 0–0.25). AZ has the same size as FA but a greater dipole moment. As a result, the resultant perovskite crystals had similar sizes but distinct optical and electronic properties. Smooth perovskite films were obtained by using combined antisolvent and low-pressure solvent annealing with trifluoromethylbenzene as antisolvent. With increasing AZ proportion, the UV/Vis absorption and PL spectra showed systematic blue shifts towards smaller wavelengths, whereas the UPS results showed a systematic downward shift of the valence-band energy levels. TCSPC measurements indicated that the rate of charge extraction increased upon increasing the AZ content. The devices were fabricated with an inverted planar heterojunction structure for $AZ_xFA_{1-x}SnI_3$ (x = 0–0.25). Upon increasing the AZ content, V_{oc} and FF increased continuously but J_{sc} decreased. The best performance occurred at x = 0.15 (AZ15), for which the best cell had J_{sc} = 21.0 mA cm^{-2}, V_{oc} = 0.65 V, FF = 0.703, and PCE = 9.6 % when the unencapsulated device was stored in air for 100 h. The AZ15 device exhibited excellent stability when the encapsulated device was stored in darkness under a N_2 environment for over 2000 h. Furthermore, when stored under ambient air (RH = 50–55 %) for over 15 days, an unencapsulated AZ15 device retained 90 % of its initial performance, which is a remarkable record for its future commercialization.

Experimental

Materials

Formamidinium iodide (FAI, Greatcell Solar), SnF_2 (99 %, Sigma-Aldrich), SnI_2 (99.999 %, Alfa Aesar), dimethyl sulfoxide (DMSO, Sigma-Aldrich) and chlorobenzene (Sigma-Aldrich) were used without purification. Azetidinium iodide (AZI) and ethylenediammonium diiodide ($EDAI_2$) were synthesized with details as follows.

Ethylenediammonium diiodide ($EDAI_2$) was prepared by the reaction of ethylenediamine (99 %, Alfa Aesar) with HI (57 wt %, 1.5 % H_3PO_2, Alfa Aesar) in an ice bath with molar ratio (1 : 2.5).

© 2021 Wiley-VCH GmbH

Excess HI was added to ensure that the reaction was complete. A white powder was precipitated in the flask, which was separated and washed with diethyl ether several times. The obtained powder was dried in a vacuum oven overnight at 50 °C.

Azetidinium iodide (AZI) was synthesized by the reaction of dilute cooled azetidine solution and HI (57 wt%, 1.5% H_3PO_2, Alfa Aesar) in 1:1 molar ratio salt-ice bath after stirring for 2 h, was dried under low pressure at 40 °C and washed with ether and recrystallized. The purity of the synthesized salt was examined with NMR spectra.

Device Fabrication

Glass substrates coated with indium tin oxide (ITO) were treated with UV-ozone for 20 min. A PEDOT:PSS layer was then spin-coated onto the ITO substrates at 5000 rpm for 50 s and dried at 160 °C for 20 min. The films were transferred into a glove box for the deposition of the perovskite layer ($O_2 \leq 2$ ppm, $H_2O \leq 0.5$ ppm). The perovskite solution of ($AZ_xFA_{1-x}SnI_3$-1% $EDAI_2$) was prepared on dissolving FAI (1-*x* mmol), AZI (*x* mmol), $EDAI_2$, (0.01 mmol), SnI_2 (1 mmol) and SnF_2 (0.1 mmol) mixed with 50 mg tin powder in DMSO (1.170 mL, 0.85 M perovskite solution) spin-coated at 5000 rpm. Chlorobenzene (800 μL), serving as antisolvent for AZ0, was dropped after 60 s of spin coating. α,α,α-trifluorotoluene (800 μL), served as antisolvent for AZ samples, was dropped after 55, 49, 40 s of spin coating for AZ5, AZ10 and AZ15, respectively. After dropping the antisolvent, the film was spun for an additional 30 s. Perovskite deposition was performed under flowing dinitrogen in a glove box to decrease the accumulation of the solvent and anti-solvent. After spin-coating, the brownish film was transferred to a hotplate (70 °C) and capped for 5 min to complete the low-pressure solvent annealing; the cap was removed to anneal for another 5 min. Solvent annealing was implemented under a low-pressure DMSO vapor solvent, which was released from the spin-coated film. Afterwards, an electron-transfer layer (C_{60}) and a hole-blocking layer (BCP) were coated with thermal evaporation (pressure 5×10^{-6} Torr, C_{60} 30 nm, BCP 5 nm). The silver back-contact electrode (100 nm) was deposited by thermal evaporation. Single crystals of AZ0, AZ10 and AZ15 were grown in saturated solutions in γ-butyl lactone at temperature 70–80 °C for 40–50 days.

Characterization of materials and devices

A field-emission scanning electron microscope (SEM, Hitachi SU8010) was used to investigate the morphology of the samples. The X-ray diffraction (XRD) patterns of the thin films coated on the ITO /PEDOT:PSS substrates and on neat glass were obtained with an X-ray diffractometer (Bruker D8). The current density-voltage characteristics of devices were recorded with a digital source meter (Keithley 2400) under one-sun illumination (AM 1.5G, 100 mW cm^{-2}) from a solar simulator (XES-40S1, SAN-E1) and were calibrated with a silicon diode and a KG-5 filter to decrease the mismatch of the spectrum. All measurements were done under ambient conditions and reverse scan (V_{oc} to 0.0 V). All devices before transfer from the glovebox were taped (Kapton tape) on the active area; some part of silver was applied to avoid touching the active area during emplacement of the metal mask. UV glue (NOA 68, Norland products) was used for encapsulation with one piece of glass slightly larger than the active area of the device. The spectra of efficiency of conversion of incident photons to current (IPCE) were recorded with a system comprising a Xe lamp (A-1010, PTi, 150 W) and a monochromator (PTi). UV/Visible absorption spectra of the perovskite samples were measured using a spectrophotometer (V780, Jasco) with an integration sphere accessory (ISN-9011, Jasco). Photoluminescence (PL) spectra were recorded using a CW diode laser (450 nm, MDL-III-450-100 mW; power supply: PSU-III-FDA) as excitation source and emission spectra recorded between 550–1100 nm on scanning the grating of a spectrometer (Dongwoo DM150i, 600 grooves, blaze: 750 nm) and detected with a TE-cooled Si photodiode (Sciencetech Inc. S-025-TE2-H; power supply: PS/TC-1). Time-correlated single-photon counting (TCSPC) measurements were performed with a TCSPC system (Fluotime 200, Picoquant) and excitation at 635 nm; transient decay profiles were collected at 840 nm. The crystallographic structures were simulated with TOPAS software (version 4.2, Bruker). Low temperature PL was recorded (Horiba JOBIN YVON iHR550 and monochromator with UV/Vis CCD) for samples excited with a 532-nm laser. A time-of-flight mass spectrometer for secondary ions enabled ION-TOF, TOF-SIMS V; Ar^+, Bi^+ were used for the analysis ion source. For single-crystal XRD, crystals grown from AZ0, AZ10 and AZ15 solutions were selected under an optical microscope and mounted on glass fibers with epoxy glue before testing. The diffraction was measured with a single-crystal X-ray diffractometer (Bruker Apex Duo system, equipped with Bruker APEX CCD) and graphite-monochromated $Mo_{K\alpha}$ radiation, $\lambda = 0.71073$ Å). Program package APEX 2 was used for structure determination and refinement. HRXRD was measured at beamline 0lC2 in National Synchrotron Radiation Research Center (NSRRC). At the sample position, the expected photon flux was 10^{11} photon/s with average resolution ($\Delta E/E$) 1.6×10^{-4}; the focused beam size was about 0.9 mm × 0.2 mm. Electrochemical impedance spectra (EIS) measurements of all devices were measured with an electrochemical workstation (IM6, Zahner, Germany) over frequency range 0.1 Hz–1 MHz with ac amplitude 10 mV under darkness. The bias voltage was switched from 0.0 V to V_{oc} for encapsulated devices. The obtained EIS data were fitted (Z-view software) based on an equivalent-circuit model. Ultraviolet photoelectron spectra and X-ray photoelectron spectra (XPS) were recorded with a surface analysis system (Thermo K-a) with the spectra calibrated with gold.

Acknowledgements

We thank Mr. Guan Ruei Chen for assistance in solving single-crystal structures, Mr. Chiung-Chi Wang (National Tsing Hua University) for TOF-SIMS measurements, and Dr. Shaham Quadir for low-temperature PL measurements. Taiwan Ministry of Science and Technology (MOST 110-2123-M-A49-001 and MOST 110-2634-F-009-026) and Center for Emergent Functional Matter Science of National Yang Ming Chiao Tung University (NYCU) from The Featured Areas Research Center Program within the framework of the Higher Education Sprout Project by Taiwan Ministry of Education (MOE) supported this research. National Synchrotron Radiation Research Center (NSRRC), Hsinchu, Taiwan, provided beam time for measurements of high resolution XRD and UPS.

Conflict of Interest

The authors declare no conflict of interest.

Keywords: antisolvent effects · azetidinium · perovskites · solar cells · tin

[1] P. Wang, Y. Wu, B. Cai, Q. Ma, X. Zheng, W.-H. Zhang, *Adv. Funct. Mater.* **2019**, *29*, 1807661.

© 2021 Wiley-VCH GmbH

[2] D. Li, D. Zhang, K. Lim, Y. Hu, Y. Rong, A. Mei, N. Park, H. Han, *Adv. Funct. Mater.* **2020**, *31*, 2008621.
[3] L. Zhang, J. Miao, J. Li, Q. Li, *Adv. Funct. Mater.* **2020**, *30*, 2003653.
[4] J. Tian, Q. Xue, Q. Yao, N. Li, C. J. Brabec, H. Yip, *Adv. Energy Mater.* **2020**, *10*, 2000183.
[5] T. Wu, D. Cui, X. Liu, X. Meng, Y. Wang, T. Noda, H. Segawa, X. Yang, Y. Zhang, L. Han, *Solar RRL* **2020**, *4*, 2000240.
[6] E. W.-G. Diau, E. Jokar, M. Rameez, *ACS Energy Lett.* **2019**, *4*, 1930–1937.
[7] J. Duan, X. Yang, Y. Duan, P. Yang, *Nano Energy* **2021**, *80*, 105526.
[8] W. Ke, C. C. Stoumpos, M. G. Kanatzidis, *Adv. Mater.* **2019**, *31*, 1803230.
[9] D. Meggiolaro, D. Ricciarelli, A. A. Alasmari, F. A. S. Alasmary, F. D. Angelis, *J. Phys. Chem. Lett.* **2020**, *11*, 3546–3556.
[10] D. Ricciarelli, D. Meggiolaro, F. Ambrosio, F. D. Angelis, *ACS Energy Lett.* **2020**, *5*, 2787–2795.
[11] R. L. Milot, M. T. Klug, C. L. Davies, Z. Wang, H. Kraus, H. J. Snaith, M. B. Johnston, L. M. Herz, *Adv. Mater.* **2018**, *30*, 1804506.
[12] S. Narra, E. Jokar, O. M. Pearce, C.-Y. Lin, A. Fathi, E. W.-G. Diau, *J. Phys. Chem. Lett.* **2020**, *11*, 5699–5704.
[13] C. B. Wang, Y. T. Zhang, F. D. Gu, Z. R. Zhao, H. S. Li, H. Jiang, Z. Q. Bian, Z. W. Liu, *Matter* **2021**, *4*, 709–721.
[14] E. Jokar, C. H. Chien, A. Fathi, M. Rameez, Y. H. Chang, E. W. G. Diau, *Energy Environ. Sci.* **2018**, *11*, 2353–2362.
[15] T. Nakamura, S. Yakumaru, M. A. Truong, K. Kim, J. Liu, S. Hu, K. Otsuka, R. Hashimoto, R. Murdey, T. Sasamori, H. D. Kim, H. Ohkita, T. Handa, Y. Kanemistu, A. Wakamiya, *Nat. Commun.* **2020**, *11*, 3008.
[16] X. Meng, T. Wu, X. Liu, X. He, T. Noda, Y. Wang, H. Segawa, L. Han, *J. Phys. Chem. Lett.* **2020**, *11*, 2965–2971.
[17] X. Liu, Y. Wang, T. Wu, X. He, X. Meng, J. Barbaud, H. Chen, H. Segawa, X. Yang, L. Han, *Nat. Commun.* **2020**, *11*, 2678.
[18] T. Wang, Q. Tai, X. Guo, J. Cao, C.-K. Liu, N. Wang, D. Shen, Y. Zhu, C.-S. Lee, F. Yan, *ACS Energy Lett.* **2020**, *5*, 1741–1749.
[19] B. Li, H. Di, B. Chang, R. Yin, L. Fu, Y. Zhang, L. Yin, *Adv. Funct. Mater.* **2021**, *31*, 2007447.
[20] E. Jokar, C. H. Chien, C. M. Tsai, A. Fathi, E. W. G. Diau, *Adv. Mater.* **2019**, *31*, 1804835.
[21] K. Nishimura, M. A. Kamarudin, D. Hirotani, K. Hamada, Q. Shen, S. Iikubo, T. Minemoto, K. Yoshino, S. Hayase, *Nano Energy* **2020**, *74*, 104858–104868.
[22] M. Rameez, S. Shahbazi, P. Raghunath, M. C. Lin, C. H. Hung, E. W.-G. Diau, *J. Phys. Chem. Lett.* **2020**, *11*, 2443–2448.
[23] B.-B. Yu, M. Liao, Y. Zhu, X. Zhang, Z. Du, Z. Jin, D. Liu, Y. wang, T. Gatti, O. Ageev, Z. He, *Adv. Funct. Mater.* **2020**, *30*, 2002230.
[24] H. Xu, Y. Jiang, T. He, S. Li, H. Wang, Y. Chen, M. Yuan, J. Chen, *Adv. Funct. Mater.* **2019**, *29*, 1807696.
[25] E. Nakanishi, R. Nishikubo, A. Wakamiya, A. Saeki, *J. Phys. Chem. Lett.* **2020**, *11*, 4043.
[26] W. Gao, C. Chen, C. Ran, H. Zheng, H. Dong, Y. Xia, Y. Chen, W. Huang, *Adv. Funct. Mater.* **2020**, *30*, 2000794.
[27] X. Liu, T. Wu, J.-Y. Chen, X. Meng, C. X. He, T. Noda, H. Chen, A. X. Yang, H. Segawa, Y. Wang, L. Han, *Energy Environ. Sci.* **2020**, *13*, 2896–2902.
[28] E. Jokar, P.-Y. Cheng, C.-Y. Lin, S. Narra, S. Shahbazi, E. W.-G. Diau, *ACS Energy Lett.* **2021**, *6*, 485–492.
[29] X. Jiang, F. Wang, Q. Wei, H. Li, Y. Shang, W. Zhou, C. Wang, P. Cheng, Q. Chen, L. Chen, Z. Ning, *Nat. Commun.* **2020**, *11*, 1245.
[30] T. Shi, H.-S. Zhang, W. Meng, Q. Teng, M. Liu, X. Yang, Y. Yan, H.-L Yip, Y.-J. Zhao, *J. Mater. Chem. A* **2017**, *5*, 15124–15129.
[31] F. Wang, J. Ma, F. Xie, L. Li, J. Chen, J. Fan, N. Zhao, *Adv. Funct. Mater.* **2016**, *26*, 3417–3423.
[32] S. R. Pering, W. Deng, J. R. Troughton, P. S. Kubiak, D. Ghosh, R. G. Niemann, F. Brivio, F. E. Jeffrey, A. B. Walker, M. S. Islam, T. M. Watson, P. R. Raithby, A. L. Johnson, S. E. Lewis, P. J. Cameron, *J. Mater. Chem. A* **2017**, *5*, 20658–20665.
[33] N. Cho, F. Li, B. Turedi, L. Sinatra, S. P. Sarmah, M. R. Parida, M. I. Saidaminov, B. Murali, V. M. Burlakov, A. Goriely, O. F. Mohammed, T. Wu, O. M. Bakr, *Nat. Commun.* **2016**, *7*, 13407.
[34] J. Liu, M. Ozaki, S. Yakumaru, T. Handa, R. Nishikubo, Y. Kanemitsu, A. Saeki, Y. Murata, R. Murdey, A. Wakamiya, *Angew. Chem. Int. Ed.* **2018**, *57*, 13221–1322; *Angew. Chem.* **2018**, *130*, 13405–13409.
[35] Z. Xiao, Q. Dong, C. Bi, Y. Shao, Y. Yuan, J. Huang, *Adv. Mater.* **2014**, *26*, 6503–6509.
[36] I. Jeon, R. Sakai, S. Seo, G. E. Morse, H. Ueno, T. Nakagawa, Y. Qian, S. Maruyama, Y. Matsuo, *J. Mater. Chem. A* **2018**, *6*, 5746–5751.
[37] H. Gunther, H. Oberhammer, *J. Mol. Spectrosc.* **1984**, *104*, 152–164.
[38] M. I. Dar, G. Jacopin, S. Meloni, A. Mattoni, N. Arora, A. Boziki, S. M. Zakeeruddin, U. Rothlisberger, M. Grätzel, *Sci. Adv.* **2016**, *2*, e1601156.
[39] H. Tan, F. Che, M. Wei, Y. Zhao, M. I. Saidaminov, P. Todorović, D. Broberg, G. Walters, F. Tan, T. Zhuang, B. Sun, Z. Liang, H. Yuan, E. Fron, J. Kim, Z. Yang, O. Voznyy, M. Asta, E. H. Sargent, *Nat. Commun.* **2018**, *9*, 3100.
[40] L. Zhou, C. Katan, W. Nie, H. Tsai, L. Pedesseau, J. J. Crochet, A. D. Mohite, S. Tretiak, A. J. Neukirch, *J. Phys. Chem. Lett.* **2019**, *10*, 3516–3524.
[41] K. T. Munson, E. R. Kennehan, G. S. Doucette, J. B. Asbury, *Chem* **2018**, *4*, 2826.
[42] S. Kahmann, S. Shao, M. A. Loi, *Adv. Funct. Mater.* **2019**, *29*, 1902963.
[43] F. Zheng, L. W. Wang, *Energy Environ. Sci.* **2019**, *12*, 1219–1230.
[44] S. Maheshwari, S. Patwardhan, G. C. Schatz, N. Renaud, F. C. Grozema, *Phys. Chem. Chem. Phys.* **2019**, *21*, 16564–16572.
[45] A. M. A. Leguy, J. M. Frost, A. P. McMahon, V. G. Sakai, W. Kochelmann, C. Law, X. Li, F. Foglia, A. Walsh, B. C. O'Regan, J. Nelson, J. T. Cabral, P. R. F. Barnes, *Nat. Commun.* **2015**, *6*, 7124.
[46] Y. Kutes, L. Ye, Y. Zhou, S. Pang, B. D. Huey, N. P. Padture, *J. Phys. Chem. Lett.* **2014**, *5*, 3335–3339.
[47] S. Tan, N. Zhou, Y. Chen, L. Li, G. Liu, P. Liu, C. Zhu, J. Lu, W. Sun, Q. Chen, H. Zhou, *Adv. Energy Mater.* **2019**, *9*, 1803024.
[48] H. Xu, Y. Sun, H. Zheng, G. Liu, X. Xu, S. Xu, L. Zhong, X. Chen, X. Pan, *J. Mater. Chem. C* **2019**, *7*, 15276–15284.
[49] J. S. Manser, M. I. Saidaminov, J. A. Christians, O. M. Bakr, P. V. Kamat, *Acc. Chem. Res.* **2016**, *49*, 330–338.

Manuscript received: July 13, 2021
Revised manuscript received: September 8, 2021
Accepted manuscript online: September 12, 2021
Version of record online: September 22, 2021

© 2021 Wiley-VCH GmbH